

The over-massive black hole in NGC 1277: New constraints from molecular gas kinematics

J. Scharwächter^{1*}, F. Combes¹, P. Salomé¹, M. Sun² and M. Krips³

¹*LERMA, Observatoire de Paris, PSL, CNRS, Sorbonne Universités, UPMC, F-75014, Paris, France*

²*Physics Department, University of Alabama in Huntsville, Huntsville, AL 35899, USA*

³*Institut de Radioastronomie Millimétrique (IRAM), 300 Rue de la Piscine, Domaine Universitaire, F-38406 Saint Martin d'Hères, France*

Accepted XXX. Received YYY; in original form ZZZ

ABSTRACT

We report the detection of CO(1-0) emission from NGC 1277, a lenticular galaxy in the Perseus Cluster, which has been proposed to host a $(1.3 - 1.7) \times 10^{10} M_{\odot}$ black hole (BH) based on stellar kinematic measurements. The CO(1-0) emission, observed with the IRAM Plateau de Bure Interferometer (PdBI) using both, a more extended (~ 1 -arcsec resolution) and a more compact (~ 2.5 -arcsec resolution) configuration, is likely to originate from the dust lane encompassing the galaxy nucleus at a distance of 0.9 arcsec (~ 320 pc). The spatially-unresolved double-horned CO(1-0) profile found at 2.5-arcsec resolution is likely to trace gas orbiting in the dust lane with rotational velocities of ~ 520 km s⁻¹, indicative of an enclosed mass of $\sim 2 \times 10^{10} M_{\odot}$. Based on models with realistic mass distributions, the CO(1-0) kinematics is found to be consistent with a $\sim 1.7 \times 10^{10} M_{\odot}$ BH, while a less massive BH is still possible assuming a large stellar mass-to-light ratio. The strongest CO(1-0) component, centred at $\sim +500$ km s⁻¹, is detected at 1-arcsec resolution. It shows an offset from the underlying continuum peak and may originate from a gas clump near the eastern orbital node of the dust lane. The extended 2.6-mm continuum emission is likely associated with a weak AGN, possibly characterized by an inverted radio-to-millimetre spectral energy distribution. Literature radio and X-ray data indicate that an ultra-massive BH in NGC 1277 would not only be over-massive with respect to the BH scaling relations, but also with respect to the fundamental plane of BH activity.

Key words: galaxies: general – galaxies: nuclei – galaxies: individual (NGC 1277) – galaxies: kinematics and dynamics

1 INTRODUCTION

The discovery of scaling relations between super-massive BHs and their host galaxies has been a major observational result in the field of galaxy evolution over the last ~ 15 –20 years. Scaling relations have been found between the mass of the super-massive BH and the stellar velocity dispersion of the host galaxy bulge ($M_{\text{BH}}-\sigma$ relation), the bulge luminosity ($M_{\text{BH}}-L_{\text{sph}}$ relation), and bulge mass ($M_{\text{BH}}-M_{\text{sph}}$ relation), (e.g. Magorrian et al. 1998; Ferrarese & Merritt 2000; Gebhardt et al. 2000; Marconi & Hunt 2003; Häring & Rix 2004; Gültekin et al. 2009a; Sani et al. 2011; Graham et al. 2011; McConnell & Ma 2013). These empirical scaling relations have been interpreted as a sign of co-evolution between super-massive BHs and their host galaxies, mediated by AGN feedback (e.g. Silk & Rees 1998; Di Matteo et al. 2005). However, the implicit build-up of scaling relations

in the course of hierarchical merging, as proposed by Peng (2007) and Jahnke & Macciò (2011), may play a role as well. A more complex picture involving self-regulatory and non-causal processes may be required to explain the various aspects of the observed BH-galaxy correlations (see Kormendy & Ho 2013, for a recent review).

Outliers from the BH scaling relations are of particular interest for the purpose of testing and interpreting these relations. Larger sample sizes of galaxies with reliable measurements of BH and galaxy parameters have recently led to refined analyses, by which it has been possible to reconcile some of the previous outliers with the BH relations. Barred galaxies have been found to deviate from the $M_{\text{BH}}-\sigma$ relation of non-barred galaxies, explaining some of the outliers with under-massive BHs (e.g. Graham 2008). Similarly, based on a classification into ‘classical’ bulges (formed by mergers) and ‘pseudo’-bulges (dominated by secular evolution and related to bars), Kormendy et al. (2011) have identified ‘pseudo’-bulges as outliers from the relations. Graham

* E-mail: julia.scharwaechter@obspm.fr

(2012) and [Graham & Scott \(2013\)](#) have recently proposed that the location of galaxies in the $M_{\text{BH}}-M_{\text{sph}}$ plane can be interpreted as a bent relation, resulting from the superposition of two different relations for galaxies with ‘Sérsic’ and ‘core-Sérsic’ spheroids in the low- and high-mass regime, respectively. ‘Core-Sérsic’ spheroids, which are typically more massive and thought to be dominated by dry mergers, follow a nearly log-linear $M_{\text{BH}}-M_{\text{sph}}$ relation, while ‘Sérsic’ spheroids, which are thought to be dominated by rapid BH growth in gas-rich processes, follow a steeper, almost quadratic relation at BH masses below $\sim (2-10) \times 10^8 M_{\odot}$. Some low-redshift AGN with apparently under-massive BHs (e.g. [Mathur et al. 2012](#); [Busch et al. 2014](#)) could be representatives of this near-quadratic relation ([Graham & Scott 2015](#)).

At the high-mass end, the BH scaling relations have recently been challenged by a number of galaxies hosting ultra-massive BHs of the order of $10^{10} M_{\odot}$, the largest BH masses known to date. Ultra-massive BHs are likely to provide new insights into galaxy and BH growth, as they must have experienced the strongest growth over time. Ultra-massive BHs seem to typically be associated with central massive galaxies in clusters. Two such galaxies, NGC 4889 and NGC 3842, have measured BH masses of $2.1_{-1.6}^{+1.6} \times 10^{10} M_{\odot}$ and $9.7_{-2.5}^{+3.0} \times 10^9 M_{\odot}$, respectively ([McConnell et al. 2011, 2012](#)) and further indirect arguments suggest a similar association ([Hlavacek-Larrondo et al. 2012](#)). Ultra-massive BHs seem to show a tendency to be over-massive compared to the $M_{\text{BH}}-\sigma$ relation, while they are still largely in agreement with the $M_{\text{BH}}-M_{\text{sph}}$ relation (cf. [McConnell & Ma 2013](#)). This deviation could indicate that the growth of the central galaxies in clusters has had a significant contribution from dry mergers, which tend to increase velocity dispersion more than stellar mass ([Volonteri & Ciotti 2013](#)). However, the dry-merger scenario is observationally controversial ([Savorgnan & Graham 2015](#)).

The most extreme case for an ultra-massive BH so far is NGC 1277, which is not a Brightest Cluster Galaxy, but a $1.2 \times 10^{11} M_{\odot}$ compact S0 galaxy in the core of the Perseus Cluster, about 3.8 arcmin away from the Brightest Cluster Galaxy NGC 1275 ([van den Bosch et al. 2012](#)). For NGC 1277, [van den Bosch et al. \(2012\)](#) find a BH mass of $(1.7 \pm 0.3) \times 10^{10} M_{\odot}$, using Schwarzschild models for the long-slit stellar kinematics and based on input photometry from multi-Gaussian expansion of a *Hubble Space Telescope* (*HST*) image. The large BH mass has recently been confirmed in a revised analysis by [Yildirim et al. \(2015\)](#), who find a marginally smaller best-fitting BH mass of $1.3 \times 10^{10} M_{\odot}$, but, otherwise, a good general agreement with the [van den Bosch et al. \(2012\)](#) results. With such a large BH mass, NGC 1277 is a significant (over-massive) outlier from the $M_{\text{BH}}-M_{\text{sph}}$ relation or the near-/mid-infrared $M_{\text{BH}}-L_{\text{sph}}$ relations and also lies above the $M_{\text{BH}}-\sigma$ relation ([van den Bosch et al. 2012](#); [Yildirim et al. 2015](#); [Ferré-Mateu et al. 2015](#)).

[van den Bosch et al. \(2012\)](#) find no strong indications that the extreme ratio of BH-to-stellar mass in NGC 1277 could be a result of stellar mass loss due to tidal stripping in the cluster environment. The stellar population of NGC 1277 is uniformly old (~ 10 Gyrs) and the galaxy shows no obvious signs of interactions ([van den Bosch et al. 2012](#); [Trujillo et al. 2014](#)). NGC 1277 has been discussed

as a local example of a ‘relic’ galaxy, which has not undergone any significant transformations in its recent evolution and shows a stellar mass density profile similar to the ones found for massive compact high-redshift galaxies ([Trujillo et al. 2014](#); [Ferré-Mateu et al. 2015](#)).

The ultra-massive BH in NGC 1277 has possibly been in place since this last violent star formation episode, because significant BH accretion without coeval star formation is unlikely ([van den Bosch et al. 2012](#)). By analysing an X-ray Chandra spectrum of NGC 1277, [Fabian et al. \(2013\)](#) find evidence of a power-law from an unresolved central point source with a 0.5–7 keV luminosity of $1.3 \times 10^{40} \text{ erg s}^{-1}$ (corrected for absorption) and extended thermal gas. NGC 1277 has also been reported to be associated with an unresolved radio continuum detection with fluxes of 2.85 and 1.6 mJy at 1.4 and 5 GHz, respectively ([Sijbring 1993](#)). [Fabian et al. \(2013\)](#) argue that the current growth rate of the BH is likely to be negligible and that radiatively efficient Bondi accretion onto such a massive BH would suggest a 5–6 orders of magnitude larger luminosity of the X-ray power-law source than observed. The small current growth rate is surprising because the X-ray properties of NGC 1277 are characteristic of minicorona and the corona lies within the Bondi radius ([Sun et al. 2007](#); [Fabian et al. 2013](#)).

In view of the extreme properties of NGC 1277, [Fabian et al. \(2013\)](#) have proposed an evolutionary scenario based on the assumption that ultra-massive BHs acquired the bulk of their mass at high redshift, where the most massive halos could grow BHs rapidly. This rapid BH growth would most likely have involved extreme AGN feedback, shutting down new star formation. By $z = 3$, ultra-massive BHs are then likely to be hosted in compact red bulges with a passive stellar population. [Fabian et al. \(2013\)](#) suggest that the further evolution of these host bulges depends on whether they are able to accrete external gas and stars. Galaxies like NGC 1277, moving at high velocity in a cluster core, may have remained virtually unchanged since $z = 3$, whilst Brightest Cluster Galaxies, centred in the cluster potential well, may have continued to grow significantly. [Graham & Scott \(2015\)](#) point out that the location of NGC 1277 in the $M_{\text{BH}}-M_{\text{sph}}$ plane overlaps with an extrapolation of the near-quadratic relation for ‘Sérsic’ spheroids to high masses, where the plane is typically populated by ‘core-Sérsic’ spheroids. In this interpretation, NGC 1277 could be a rare example of a galaxy in which growth by gas-rich processes has continued on a near-quadratic relation instead of being terminated at the typical break mass. This scenario, however, is more difficult to reconcile with the small present growth rate of the BH in NGC 1277 and the lack of recent star formation.

It has been controversially discussed whether a BH mass above $10^{10} M_{\odot}$ is indeed necessary to explain the observed stellar kinematics of NGC 1277. [Emsellem \(2013\)](#) argues that this large value for the BH mass is mostly determined by the fit to the central part of the measured Gauss-Hermite h_4 profile, so that the accuracy of this parameter is critical. The N-body realisations presented by [Emsellem \(2013\)](#) show that a much smaller BH mass of $5 \times 10^9 M_{\odot}$ provides a good fit of the stellar kinematics, except for a small discrepancy in the Gauss-Hermite h_4 parameter. An even smaller BH mass is possible, if variations in the mass-to-light ratio or high-velocity stars in the central region are present. These

N-body realisations are based on a new multi-Gaussian expansion of the *HST* photometry and on the assumption that the potential is defined by a constant mass-to-light ratio of $M/L_V = 10$ without any dark matter halo. As an alternative scenario, Emsellem (2013) also demonstrates that an end-on view on an inner bar together with a BH of only $2.5 \times 10^9 M_\odot$ can reproduce the stellar kinematics, except for the central part of the h_4 profile. The smaller BH masses would bring NGC 1277 close to or even into agreement with the BH scaling relations.

An independent constraint on whether the centre of NGC 1277 could harbour an over-massive BH can be obtained by using gas kinematics as a tracer of the gravitational potential (e.g. Davis 2014). In this paper, we report the first detection of CO(1-0) emission from the centre of NGC 1277, based on observations with the IRAM PdBI. We interpret the CO(1-0) and 2.6-mm continuum data with the help of an optical image, obtained from archival *HST* data, and discuss implications for the BH mass of NGC 1277. The observations and data reduction of the IRAM and ancillary data are described in Section 2. The results obtained for the CO(1-0) and 2.6-mm continuum emission are presented in Section 3. In Section 4, we interpret the origin of the molecular gas and continuum detections, derive constraints for the enclosed mass from the molecular gas kinematics, and discuss BH accretion scenarios. We summarise the main results in Section 4 and conclude with notes on the role of NGC 1277 in BH and galaxy growth scenarios. Throughout the paper, we will assume a scale of $353 \text{ pc arcsec}^{-1}$ and a luminosity distance modulus of 34.39 (i.e. a luminosity distance of 75.5 Mpc), consistent with the values used by van den Bosch et al. (2012).

2 OBSERVATIONS AND DATA REDUCTION

2.1 IRAM PdBI data

The millimetre data for NGC 1277 were obtained using the IRAM PdBI in both, a more extended and a more compact configuration, providing spatial resolutions of ~ 1 arcsec and ~ 2.5 arcsec, respectively. In order to observe the redshifted CO(1-0) line in NGC 1277, the dual-polarisation receiver in the 3-mm band was tuned to 113.356 GHz, according to the optical systemic velocity of NGC 1277 of 5066 km s^{-1} (Falco et al. 1999). We verified the systemic velocity based on stellar absorption lines (Ca I $\lambda 2.26 \mu\text{m}$, Mg I $\lambda 2.28 \mu\text{m}$, and CO bandheads at about 2.29, 2.32, and $2.35 \mu\text{m}$) in a single nuclear-aperture *K*-band spectrum of NGC 1277, extracted from a subset of archival NIFS (Gemini North) data from program GN-2011B-Q-27 (PI: D. Richstone). The systemic velocity derived from fitting this spectrum with template stars from the NIFS spectral template library v2.0 (Winge et al. 2009) using PPF (Cappellari & Emsellem 2004) agrees within $\sim 20 \text{ km s}^{-1}$ with the value of 5066 km s^{-1} . Since an offset of this order of magnitude is negligible compared to the accuracy at which the CO(1-0) data are analysed, we will present the CO(1-0) data using the reference velocity of 5066 km s^{-1} .

The PdBI observations of NGC 1277 were performed using the Wide-Band correlator WideX, which provides a spectral resolution of 1.95 MHz and a bandwidth of 3.6 GHz

covering the CO(1-0) line as well as the adjacent 2.6-mm continuum. The J2000 coordinates R.A. = 03h 19m 51.5s and Dec = $+41^\circ 34' 24''.7$ were used as pointing reference. The data for both configurations were reduced using the IRAM GILDAS software CLIC and MAPPING.

2.1.1 Observations at high spatial resolution

In the more extended configuration (B configuration), NGC 1277 was observed on 2014 March 12 and 2014 March 14, respectively. These observations covered baselines between 88 and 452 m and a total on-source time of 8.29 h with six antennae. The phase and amplitude calibration for both observing dates was derived from observations of 3C 84 and quasar 0307+380. For the data from 2014 March 12, 3C 273 was used as RF calibrator, while quasar 0307+380 was used as flux calibrator. For the data from 2014 March 14, these calibrations were performed based on quasar 2013+370 and MWC349, respectively. The final UV table was created by merging the data from both observing dates.

The UV table was converted into a data cube by mapping the data spatially onto 512×512 pixels using natural weighting, no tapering, and a pixel size of $0.24 \times 0.24 \text{ arcsec}^2$. The data were binned to a spectral resolution of 10 MHz or (26.4 km s^{-1}), resulting in 360 channels. The data cube was cleaned by applying Högbom deconvolution (Högbom 1974) to each spatial plane. The deconvolution was performed with a predefined support covering the emission that is evident in each channel close to the reference position of NGC 1277. The resulting beam size in this more extended configuration is $1.1 \times 0.83 \text{ arcsec}^2$. The 1σ noise level per 10-MHz channel in the cleaned cube increases with decreasing velocity from about $0.6 \text{ mJy beam}^{-1}$ at 6000 km s^{-1} to $1.1 \text{ mJy beam}^{-1}$ at -3400 km s^{-1} with a value of $0.83 \text{ mJy beam}^{-1}$ around the NGC 1277 reference velocity.

Since the CO(1-0) emission in this data set is weak, a blind detection assessment was performed on the cleaned data cube, both before and after continuum subtraction, using a wrapper around SExtractor (Bertin & Arnouts 1996). For each channel in the cube, a narrow-band image was created by averaging over a predefined number of neighbouring channels. In order to account for different line widths, the channel average was varied between a single channel and the maximum range of channels, using only odd numbers for a symmetric average around the central channel. Each narrow-band image was sent to SExtractor in order to identify all groups of pixels with values above a certain detection threshold. Both, the detection threshold as well as the minimum area covered by pixels above this threshold, are user-defined input parameters of SExtractor. In order to improve the detection process, we applied the SExtractor image filtering before detection, using a Gaussian convolution kernel with an FWHM of 4 pixels (0.96 arcsec), which roughly matches the beam size.

The detection assessment of the full data cube using single-channel narrow-band images, a SExtractor detection threshold of 3σ , and a minimum detection area of 3 pixels, results in the detection of a continuum emission peak at a mean offset of $\Delta\text{R.A.} = -0.14 \text{ arcsec}$ and $\Delta\text{Dec} = 0.18 \text{ arcsec}$ for most channels across the full frequency range. In order to isolate weak line emission, a continuum subtraction was applied to the data cube. For this step, the continuum

was extracted by averaging all channels outside the velocity range from -800 to $+800$ km s^{-1} around the reference velocity where line emission from NGC 1277 may be expected. The resulting continuum image has a 1σ background noise level of 0.078 mJy beam^{-1} . A new detection assessment was performed on the continuum-subtracted data cube, using a detection threshold of 2.5σ and a minimum detection area of 1 pixel to detect faint features. Within a distance of 15 arcsec and a velocity interval of ± 800 km s^{-1} around the reference position and velocity, respectively, only one detection is identified at a $> 5\sigma$ (peak flux over background rms) level. This detection at 5.1σ is found at $\Delta\text{R.A.} = 0.48$ arcsec and $\Delta\text{Dec} = 0.24$ arcsec from the reference position when averaging 9 channels (238 km s^{-1}) around a central velocity of $+503$ km s^{-1} . While this detection is rather marginal based on the blind assessment, we will show in Sect. 3.3 that this feature is clearly confirmed as CO(1-0) emission from NGC 1277 by comparison with the data obtained at lower spatial resolution.

2.1.2 Observations at low spatial resolution

The data in the more compact configuration (special C configuration, including the new seventh antenna) were observed on 2014 December 16 using six antennae, and on 2015 February 19 and 2015 April 11 using seven antennae, respectively. The observations covered baselines between 24 and 176 m and an on-source time of 5.77 h for seven antennae.

The phase and amplitude calibration for all observing dates is based on 3C 84 and quasar 0300+470. The RF calibrators are 3C 454.3 for 2014 December 16 and quasar 0059+581 for 2015 April 11. While 3C 84 may have CO(1-0) emission, it was nevertheless chosen as RF calibrator for 2015 February 19. No obvious contamination was found and the RF calibration was improved by using this strong source instead of the weaker alternatives. The final UV table was created by merging the data from all observing dates using a spectral resolution of 40 MHz (106 km s^{-1}).

The UV table was mapped using 256×256 spatial pixels, natural weighting, no tapering, and a pixel size of 0.62×0.62 arcsec². The data cube was cleaned using the same method as applied to the high-resolution data. The resulting beam size is 2.62×2.31 arcsec². The 1σ noise level per 40-MHz channel in the cleaned cube is found to be 0.42 mJy beam^{-1} at 6000 km s^{-1} and increases to 0.7 mJy beam^{-1} at -3400 km s^{-1} with a value of about 0.57 mJy beam^{-1} around the NGC 1277 reference velocity. The continuum was subtracted from the cleaned data cube by subtracting the average of all channels close to the line emission but excluding the velocity range of the line itself. A number of the highest and lowest velocity channels were not considered when computing the continuum, since they show possible indications of unidentified peaks close to -3000 and $+5000$ km s^{-1} .

2.2 Ancillary optical data

Ancillary archival data from *HST* observations in the *F550M* filter are used to compare the millimetre observations with the optical features of NGC 1277. The optical *HST* image has already been presented by other authors to

discuss the morphology of NGC 1277 (van den Bosch et al. 2012; Fabian et al. 2013; Emsellem 2013; Trujillo et al. 2014). We found the World Coordinate System (WCS) of the archival *HST* image to be offset, which we corrected by comparing the positions of objects in a $\sim 45 \times 45$ arcsec² cut-out around NGC 1277 to coordinates from the Guide Star Catalog (GSC) 2.3 (Lasker et al. 2008). Four of these objects, extracted using the IMSTAR routine included in the WCSTOOLS package (e.g. Mink 1997), were found to match catalogued sources. Based on these, a new plate solution was derived using the IRAF¹ task CCMAP with a second-order polynomial fit. The fit shows an rms of about 0.2 arcsec, which is a similar order of magnitude as the average absolute astrometry error of 0.2–0.3 arcsec of the GSC 2.3 (Lasker et al. 2008). The *HST* image was resampled according to the new plate solution onto 0.05×0.05 arcsec² pixels using the software SWARP (Bertin et al. 2002) with a LANCZOS3 interpolation and an oversampling factor of 3. The final image quality, based on stars in the image field-of-view, is ~ 0.14 – 0.15 arcsec (Gaussian FWHM).

3 RESULTS

3.1 Optical morphology

As already discussed by other authors (van den Bosch et al. 2012; Fabian et al. 2013; Emsellem 2013), the *HST* optical image shows a prominent dust lane around the centre of NGC 1277 (Fig. 1). The dust lane has a radius of ~ 0.9 arcsec (~ 320 pc), (see also, e.g., Fabian et al. 2013), and is seen nearly edge-on. van den Bosch et al. (2012) deduce an inclination of $\sim 75^\circ$, suggesting a similar inclination for the galaxy, if the dust lane is in the plane of the galaxy disk. It has been noted by Fabian et al. (2013) that the large central mass concentration corresponding to a $\sim 10^{10} M_\odot$ BH in NGC 1277 would imply high circular velocities of 480 km s^{-1} for gas orbiting in the dust lane.

3.2 2.6-mm continuum emission

The 2.6-mm continuum of NGC 1277 (Fig. 2), derived by averaging all channels outside -800 and $+800$ km s^{-1} around the reference velocity in the high-spatial-resolution data, shows an integrated flux of (5.95 ± 0.05) mJy in a circular aperture with a radius of 7 pixels (1.68 arcsec). The continuum is found to be extended at the spatial resolution of 1 arcsec. In order to probe the continuum extension, both, a point source and a circular Gaussian model, were fitted to the continuum map after convolution of the models with the beam. Both models result in $\Delta\text{R.A.} = -0.14$ arcsec and $\Delta\text{Dec} = 0.18$ arcsec for the continuum position with respect to the pointing reference. This is in agreement with the position derived from the basic blind detection assessment in Sect. 2.1.1. Fitting a point source model, yields a best-fitting flux of $S = 4.75$ mJy. It is obvious that this fit only recovers about 80 per cent of the total flux of 5.95 mJy, obtained

¹ IRAF is distributed by the National Optical Astronomy Observatories, which are operated by the Association of Universities for Research in Astronomy, Inc., under cooperative agreement with the National Science Foundation.

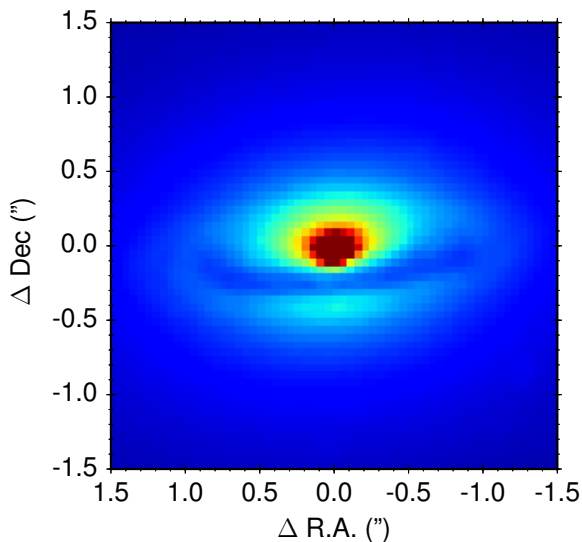


Figure 1. Optical $F550M$ *HST* image of the central 3×3 arcsec² region of NGC 1277. The image is shown in arbitrary units. The chosen colour scale does not properly represent the full spatial resolution of the data, but has been adjusted to enhance the contrast on the dust lane. The centre of the relative coordinate system is determined from a Gaussian fit to the nuclear emission peak.

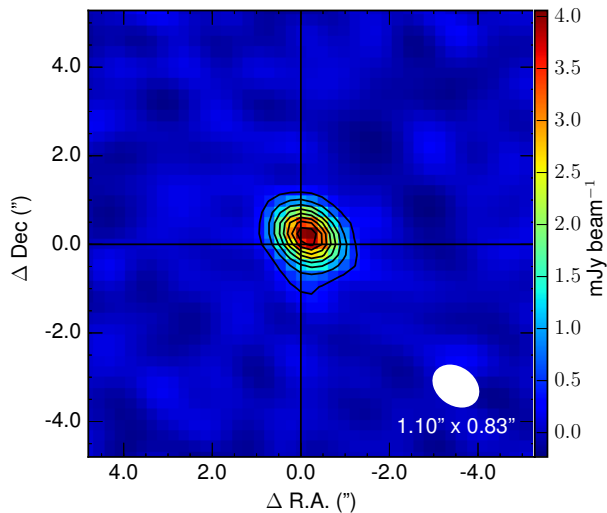


Figure 2. Map of the 2.6-mm continuum of NGC 1277 based on the data obtained in the more extended configuration. Contour levels start at 5σ and are shown in steps of 6σ (at 0.39, 0.86, 1.33, 1.79, 2.26, 2.73, 3.20, 3.67 mJy beam⁻¹). The colour scale extends from -3σ to the continuum peak value. The size and orientation of the beam are indicated in the lower right corner.

by direct aperture integration. The residual map of the continuum after subtraction of the point-source model (Fig. 3, top panel) shows that the continuum has extended excess emission compared to a point source. Fitting a single circular Gaussian instead of a point source, yields best-fitting parameters of $S = 5.71$ mJy for the flux and 0.6 arcsec for the Gaussian FWHM. The circular Gaussian model recov-

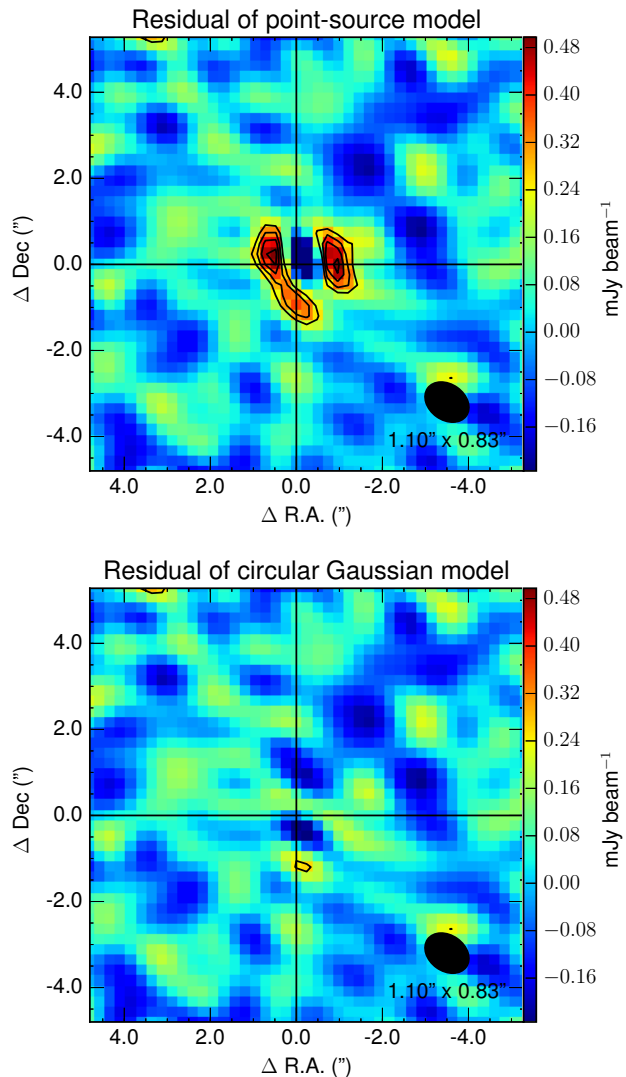


Figure 3. Residual maps after subtracting a point source model (top) and a circular Gaussian model (bottom) from the 2.6-mm continuum of NGC 1277, based on the high-resolution data. The 1σ noise level of the maps is 0.078 mJy beam⁻¹. Contour levels start at 3σ and are shown in steps of 1σ (at 0.23, 0.31, 0.39, 0.47, and 0.55 mJy beam⁻¹). The colour scale in both plots is identical and ranges between -3σ and the peak value of the map in the top panel. The size and orientation of the beam are indicated in the lower right corner.

ers most of the flux measured via direct aperture integration. The residuals (Fig. 3, bottom panel) are negligible, except for a possible weak excess emission to the south which is found at the 3σ -level.

3.3 CO(1-0) emission

A very broad CO(1-0) line is clearly detected close to the pointing reference in the low-spatial-resolution data (Figs 4 and 5). The line is symmetrically centred around the systemic velocity of NGC 1277. It covers a wide spectral range of about 1480 km s⁻¹ and shows indications of a double-

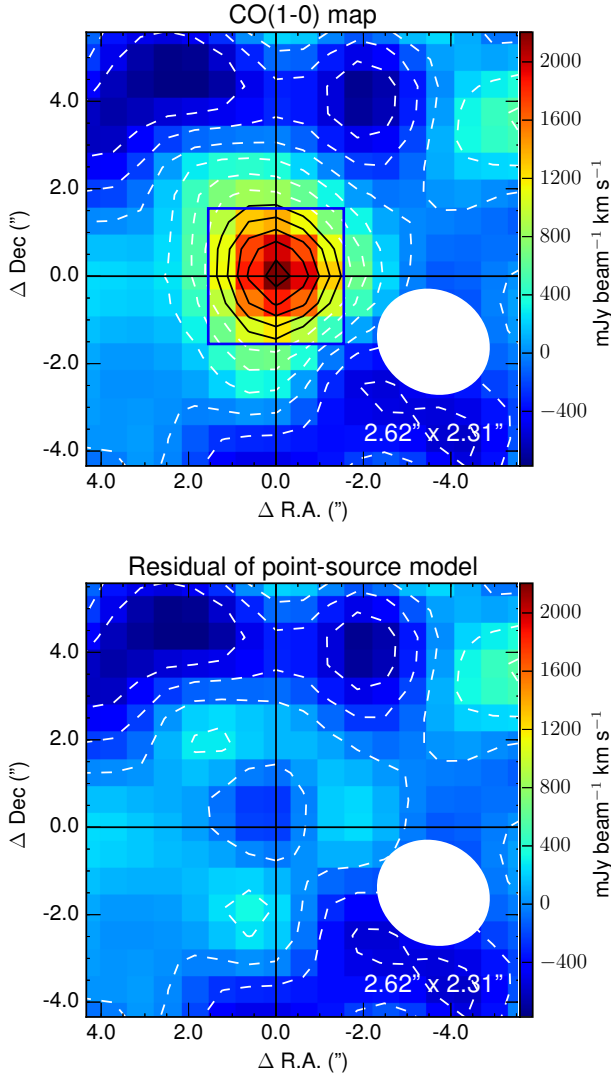


Figure 4. Map of the CO(1-0) detection for NGC 1277 obtained in the more compact configuration (top panel) and residual map after subtracting a beam-convolved point-source model (bottom panel). The CO(1-0) line has been integrated over a velocity range of 1480 km s^{-1} (14 channels of 40 MHz). The 4σ to 8σ contours (1033, 1292, 1550, 1808, and $2067 \text{ mJy beam}^{-1} \text{ km s}^{-1}$) are shown as black solid lines. The -3σ to 3σ contours (-775 , -517 , -258 , 0.0 , 258 , 517 , and $775 \text{ mJy beam}^{-1} \text{ km s}^{-1}$) are shown as dashed white lines. The size and orientation of the beam are indicated in the lower right corner. Direct integration over 5×5 pixels, i.e. $3.1 \times 3.1 \text{ arcsec}^2$ (blue box) provides a total flux of $(1850 \pm 70) \text{ mJy km s}^{-1}$.

horned profile with a stronger velocity component centred at $+500 \text{ km s}^{-1}$ and a less pronounced component centred at -500 km s^{-1} (Fig. 5). The corresponding CO(1-0) map, shown in Fig. 4, has been integrated spectrally over 14 channels of 40-MHz width (1480 km s^{-1}), as indicated by the vertical dashed lines in Fig. 5. The total flux of the CO(1-0) line, integrated over the area marked in Fig. 4, is $(1850 \pm 70) \text{ mJy km s}^{-1}$. Fitting a point source model to the CO(1-0) map results in a source at $\Delta \text{R.A.} = 0.06 \text{ arcsec}$ and

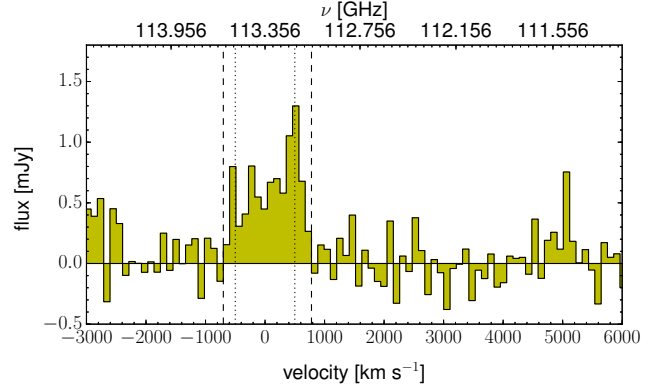


Figure 5. CO(1-0) spectrum obtained for NGC 1277 in the more compact configuration. The spectrum, with a resolution of 40 MHz, is extracted from the central 3×3 brightest pixels of the CO emission peak, as shown in Fig. 4. The emission map in Fig. 4 was integrated over the spectral range indicated by the vertical dashed lines. The vertical dotted lines mark $+500$ and -500 km s^{-1} , which roughly coincides with the peak of the double-horned line profile. The spectrum is shown for the full spectral range provided by the observations, including the two unidentified peaks near -3000 and 5000 km s^{-1} that were omitted from the channel average used to compute and subtract the continuum (see Sect. 2.1.2).

$\Delta \text{Dec} = 0.15 \text{ arcsec}$ with a flux of $2450 \text{ mJy km s}^{-1}$. The residuals from this fit are negligible (Fig. 4, bottom panel), suggesting that the CO(1-0) emission is virtually unresolved at 2.5-arcsec resolution.

At 1-arcsec resolution, in the more extended configuration, only the pronounced velocity component at $+500 \text{ km s}^{-1}$ is detected. This component corresponds to the emission found via the blind detection assessment described in Sect. 2.1.1. The narrow-band image of this single CO(1-0) detection is presented in the top panel of Fig. 6. This image has been averaged over 9 channels (238 km s^{-1}) to isolate the line emission, as suggested by the detection experiment (Sect. 2.1.1). Fig. 7 shows the corresponding CO(1-0) spectrum, obtained by spatially integrating the CO emission over a 4×4 pixel box ($0.96 \times 0.96 \text{ arcsec}^2$) around the CO emission peak, as indicated by the blue box in Fig. 6 (top panel). The total flux obtained for the 9-channel-wide line when integrating over 4×4 pixels ($0.96 \times 0.96 \text{ arcsec}^2$) is $(180 \pm 10) \text{ mJy km s}^{-1}$.

The CO(1-0) component detected at 1-arcsec resolution is found to be spatially unresolved. The residuals after fitting the CO(1-0) emission shown in Fig. 6 (top panel) with a point-source model convolved with the beam are negligible (bottom panel in the same Figure). The fit yields best-fitting parameters of $\Delta \text{R.A.} = 0.48 \text{ arcsec}$ and $\Delta \text{Dec} = 0.20 \text{ arcsec}$ for the offset with respect to the pointing reference position, which is very similar to the offset found by the blind detection assessment (Sect. 2.1.1). The flux recovered by fitting the point-source model is $S = 310 \text{ mJy km s}^{-1}$, i.e. larger than the flux obtained from direct integration over the 4×4 pixel box ($0.96 \times 0.96 \text{ arcsec}^2$) shown in the top panel of Fig. 6.

Along the spectral axis (Fig. 7), the CO(1-0) line profile is offset by $+510 \text{ km s}^{-1}$ from the systemic velocity of NGC 1277. The line profile, as derived from fitting a single

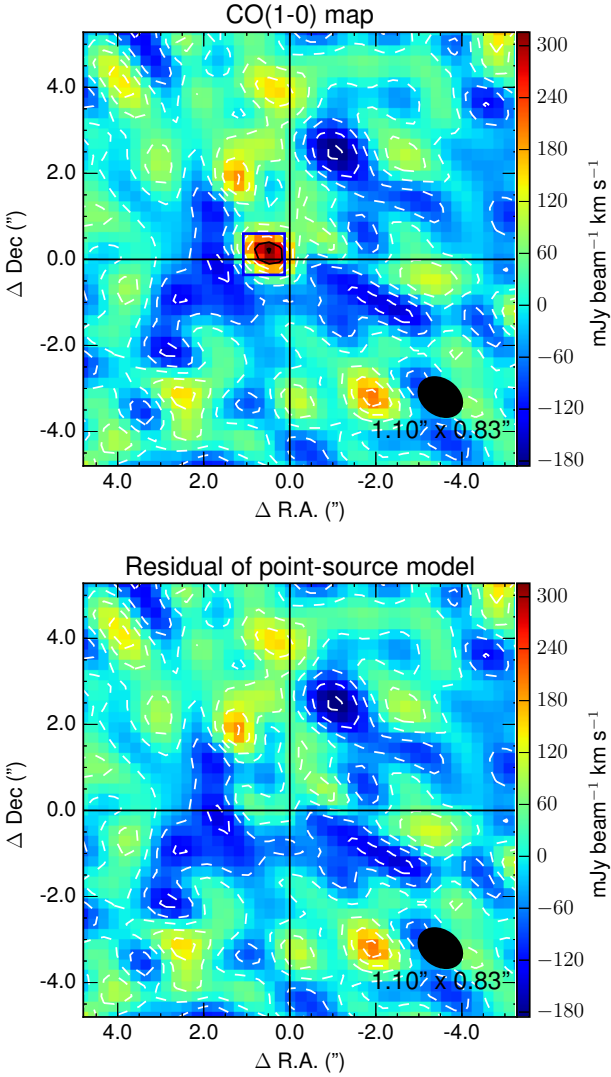


Figure 6. Map of the CO(1-0) detection for NGC 1277 (top panel) in the more extended configuration and residual map after subtracting a beam-convolved point-source model (bottom panel). The CO(1-0) line has been integrated over a velocity range of 238 km s^{-1} (9 channels of 10 MHz). The 4σ and 5σ contours (248 and $309 \text{ mJy beam}^{-1} \text{ km s}^{-1}$) are shown as black solid lines. The -3σ to 3σ contours ($-186, -124, -62, 0.0, 62, 124, 186 \text{ mJy beam}^{-1} \text{ km s}^{-1}$) are shown as dashed white lines. The size and orientation of the beam are indicated in the lower right corner. The blue box in the top panel indicates the 4×4 pixel box ($0.96 \times 0.96 \text{ arcsec}^2$) that was used to spatially integrate the spectrum shown in Fig. 7.

Gaussian function (red line in Fig. 7), has a width of $(80 \pm 20) \text{ km s}^{-1}$ (Gaussian sigma, i.e. $(190 \pm 50) \text{ km s}^{-1}$ FWHM). The line fluxes resulting from the Gaussian fit or direct integration over the 9 channels are $(190 \pm 60) \text{ mJy km s}^{-1}$ and $(180 \pm 50) \text{ mJy km s}^{-1}$, respectively, in agreement with the above value obtained from the CO(1-0) map.

In addition to the velocity offset, the spatially-unresolved $+500 \text{ km s}^{-1}$ CO(1-0) component in the 1-arcsec resolution data shows a spatial offset of 0.6 arcsec to the

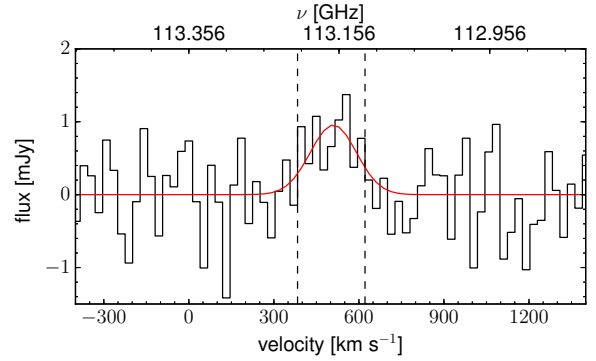


Figure 7. Spectrum of the CO(1-0) detection in the more extended configuration. The spectrum has been integrated over a 4×4 pixel box ($0.96 \times 0.96 \text{ arcsec}^2$) around the CO emission peak, as shown in Fig. 6. The CO(1-0) line profile is fitted with a single Gaussian function (red line), resulting in a flux of $(190 \pm 60) \text{ mJy km s}^{-1}$, a line centre at $(510 \pm 20) \text{ km s}^{-1}$, and a Gaussian sigma of $(80 \pm 20) \text{ km s}^{-1}$ (where the reported errors have been determined via Monte Carlo simulations). The vertical dashed lines indicate the spectral region of the 9 channels of 10 MHz (238 km s^{-1}) over which the line was integrated in order to create the emission map in Fig. 6.

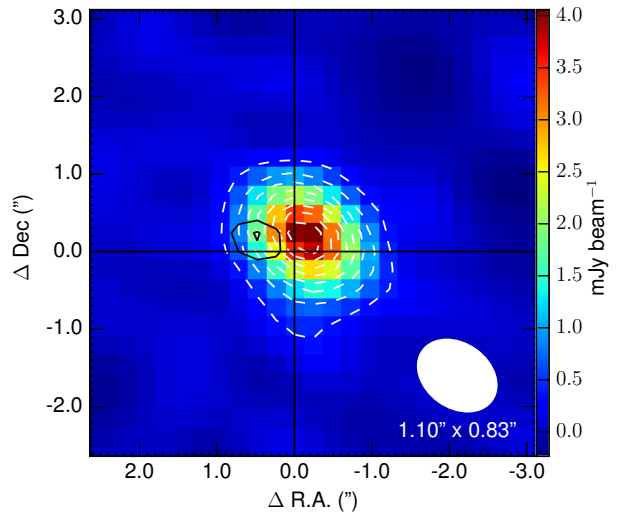


Figure 8. Position of the CO(1-0) emission relative to the 2.6-mm continuum emission in the high resolution data. The continuum colour scale and contours (white dashed lines) are the same as in Fig. 2. The two CO(1-0) contours (black solid lines) are the same 4 and 5σ contours as shown in Fig. 6. The size and orientation of the beam are indicated in the lower right corner.

east compared to the 2.6-mm continuum emission (Fig. 8). Assuming that the 1σ positional uncertainty $\Delta\theta$ for a signal-to-noise ratio SNR and a beam size Θ_B is given by $\Delta\theta \approx \Theta_B / (2 \times \text{SNR})$, the CO(1-0) line emission involves a positional uncertainty of $\Delta\theta \sim 0.1 \text{ arcsec}$ (using the major axis of the beam size ($\sim 1.1 \text{ arcsec}$) and the SNR of the CO(1-0) emission peak of ~ 5.1). Compared to this estimate, the measured offset between the CO(1-0) and 2.6-mm continuum emission has a $\sim 6\sigma$ significance. (For the continuum peak, the uncertainty is much smaller than 0.1 arcsec , as it is detected with a much larger SNR.) It is also noteworthy that the direction of the offset of the CO(1-0) emission

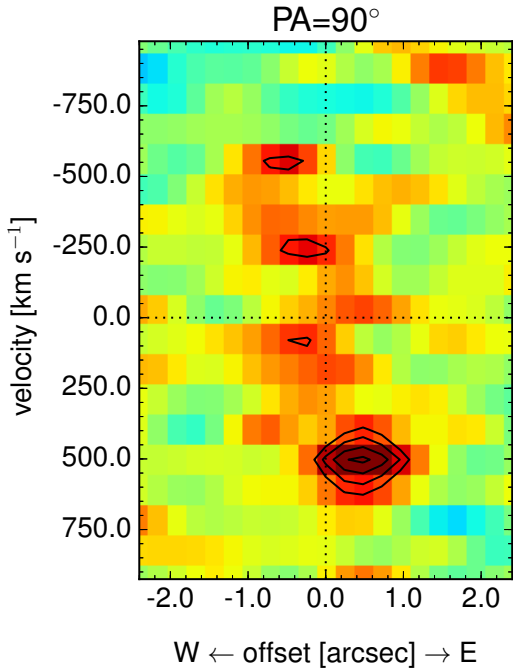


Figure 9. Position-velocity diagram of the CO(1-0) emission, extracted along a 0.72-arcsec-wide slit oriented in east-west direction and centred on the position defined by the peak of the 2.6-mm continuum. The diagram is based on the combined data set of all CO(1-0) observations discussed in this paper. This merged data set has a beam size of 1.3×1.0 arcsec² with a major axis orientation along PA = 52° and is shown at a spectral resolution of 40 MHz (106 km s⁻¹) after continuum subtraction. Contours start at 4σ and increase in steps of 1σ .

with respect to the 2.6-mm continuum peak does not coincide with the possible weak extension of the continuum to the south, mentioned in Section 3.2.

Marginal evidence of a spatial gradient across the CO(1-0) kinematic components in east-west direction is found in the combined data set after merging the 1-arcsec and 2.5-arcsec resolution data. The position-velocity diagram extracted from this merged data set along a slit oriented in east-west direction is shown in Fig. 9. Apart from the dominant +500 km s⁻¹ component, the CO(1-0) emission is characterized by a low signal-to-noise ratio in this spatially-resolved diagram. However, the diagram indicates that the highest-velocity (+500 km s⁻¹) component is located farthest to the east, while the lowest-velocity components around -500 km s⁻¹ are found farthest to the west. A spatial gradient between these extreme velocity components would be consistent with molecular gas clumps in rotation around a north-south axis.

4 DISCUSSION

4.1 Origin of the 2.6-mm continuum emission

The 2.6-mm continuum flux of NGC 1277 of (5.95 ± 0.05) mJy could be associated with star formation or with an AGN-related radio jet. In order to discuss the origin of this

continuum emission, we show the 2.6-mm continuum flux together with the infrared-to-radio spectral energy distribution of NGC 1277 in Fig. 10. The analysis of the spectral energy distribution is likely to involve uncertainties given that the composite is based on an inhomogeneous data set. Furthermore, the significance of the models discussed in the following is limited by the small number of published data at radio frequencies. To our knowledge, the only published data in the radio domain are the 1.4 and 5 GHz detections of 2.85 and 1.6 mJy, respectively, reported by Sijbring (1993), who found the radio source to be unresolved in the corresponding 13×19 arcsec² and 3.5×5.2 arcsec² beams.

Fig. 10 shows example models for the available data, based on the far-infrared and radio continuum, which underpredict the flux at 2.6-mm by about one order of magnitude. The infrared data include data from *Herschel*, *Spitzer*, and *Wise*. The *Herschel* photometry measurement was performed using the Herschel Interactive Processing Environment (HIPE) 13.0.0. The SPIRE fluxes are from SUSSEXTRACTOR, while the results from the TIMELINE FITTER agree within a few per cent. The PACS fluxes are derived from aperture photometry with aperture correction included. We used the python code MBB_LEMCEE to fit modified blackbodies to photometry data using an affine invariant Markov chain Monte Carlo (MCMC) method, with the *Herschel* passband response folded (Dowell et al. 2014). Assuming that all dust grains share a single temperature T_d , that the dust distribution is optically thin, and neglecting any power-law component towards shorter wavelengths, the fit results in a temperature of $T_d/(1+z) = (24.0 \pm 0.8)$ K, a luminosity $L_{\text{IR}}(8-1000 \mu\text{m}) = (2.3 \pm 0.2) \times 10^9 L_\odot$, and a dust mass of $M_d = (2.6 \pm 0.5) \times 10^6 M_\odot$ for $\beta = 2$. For $\beta = 1.5$, the corresponding values are $T_d/(1+z) = (27 \pm 1)$ K, $L_{\text{IR}}(8-1000 \mu\text{m}) = (2.4 \pm 0.2) \times 10^9 L_\odot$, and $M_d = (1.3 \pm 0.2) \times 10^6 M_\odot$. We also performed a fit using a free β parameter, which results in $T_d/(1+z) = (32 \pm 5)$ K, $L_{\text{IR}}(8-1000 \mu\text{m}) = (2.4 \pm 0.2) \times 10^9 L_\odot$, $M_d = (9 \pm 5) \times 10^5 M_\odot$, and $\beta = 1.1 \pm 0.4$. These temperatures are similar to the ones found for the cold dust component in galaxies, which has been interpreted as diffuse dust heated by the general interstellar radiation field from young and/or old stellar populations (e.g. Cox et al. 1986). Given that NGC 1277 has been found to host a uniformly old stellar population (van den Bosch et al. 2012; Trujillo et al. 2014), heating by the general interstellar radiation field is a likely explanation for the observed far-infrared fluxes. The cold dust component alone can clearly not account for the continuum emission found at 2.6 mm.

The radio fluxes at 1.4 and 5 GHz have been fitted with a single power-law of the form $S_\nu \propto \nu^\alpha$, resulting in a power-law index of $\alpha = -0.46$. This index is in agreement with a synchrotron spectrum. Regarding the lack of evidence for recent star formation in NGC 1277 (van den Bosch et al. 2012; Trujillo et al. 2014), it is possible that the 1.4 and 5 GHz data trace non-thermal emission from an extended radio jet. This conclusion is also supported by the fact that the given radio and far-infrared fluxes indicate a mild radio excess with respect to the radio-far-infrared relation for star forming galaxies. Based on the definition

$$q = \log \left[\frac{S_{\text{FIR}}}{3.75 \times 10^{12} \text{ W m}^{-2}} \right] - \log \left[\frac{S_{1.4 \text{ GHz}}}{\text{W m}^{-2} \text{ Hz}^{-1}} \right] \quad (1)$$

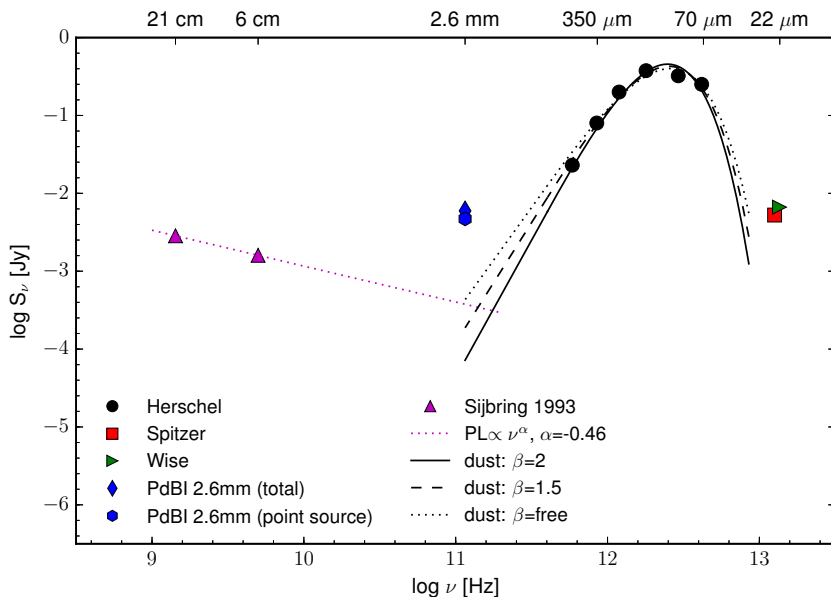


Figure 10. Infrared-to-radio spectral energy distribution of NGC 1277, together with an example model fit based on the far-infrared and radio data (see text for details). The infrared measurements are compiled based on data from *Herschel*, *Spitzer*, and *Wise*, as described in the text. For the 2.6-mm continuum measured in this work the figure shows both, the total aperture-integrated flux as well as the point source contribution discussed in Sect. 3.2. The 1.4 and 5 GHz fluxes are taken from Sijbring (1993). The solid, dashed, and dotted black lines show the fits for the dust component, assuming $\beta = 2$, $\beta = 1.5$, and a free β , as described in the text. The dotted magenta line shows the results from fitting a power-law $S_\nu \propto \nu^\alpha$ to the 1.4 and 5 GHz fluxes.

with $S_{\text{FIR}} = 1.26 \times 10^{-14} [2.58 S_{60 \mu\text{m}} + S_{100 \mu\text{m}}] \text{ W m}^{-2}$ from Yun et al. (2001), the 70 and 100 μm fluxes for NGC 1277 from *Herschel* and the 1.4 GHz flux from Sijbring (1993) suggest $q \sim 2.0$. A comparison with figure 6 in Yun et al. (2001) shows that this q -value indicates some radio excess compared to the distribution of q -values for far-infrared selected galaxies and, therefore, a possible contribution from an AGN.

The excess of the 2.6-mm continuum in Fig. 10 (both, when considering the total flux or only the point source contribution) with respect to the synchrotron-like radio continuum derived from the 1.4 and 5 GHz fluxes of NGC 1277 is about one order of magnitude. Regarding the uniformly old stellar population in NGC 1277 (van den Bosch et al. 2012; Trujillo et al. 2014), free-free emission from HII regions is unlikely to account for the full 2.6-mm excess. It is also possible that NGC 1277 harbours an AGN with a rather flat or inverted spectral energy distribution from the radio to the millimetre regime. Some of this excess could be caused by variability or by extended non-thermal emission probed more prominently by the larger beam size corresponding to the 1.4 and 5 GHz data. Similarly inverted spectra have been found for a number of low-luminosity AGN and elliptical galaxies (Doi et al. 2005, 2011). These authors discuss the possibility that the strong flux at millimetre wavelengths is a signature of the accretion disc in an advection-dominated accretion flow (Ichimaru 1977). More data at radio and millimetre wavelengths will be required for a more stringent interpretation of the radio-to-millimetre spectral energy distribution of NGC 1277.

The presence of a weak AGN in NGC 1277 would be consistent with X-ray data. Fabian et al. (2013) find evi-

dence for an unresolved power-law source with a 0.5–7 keV luminosity of $1.3 \times 10^{40} \text{ erg s}^{-1}$. A rough estimate indicates that an AGN producing the X-ray and the non-thermal radio emission would be in agreement with the known radio-X-ray correlations for AGN. The 6-cm (5 GHz) flux of $S_{6 \text{ cm}} = 1.6 \text{ mJy}$ from Sijbring (1993) corresponds to a luminosity of $L_{6 \text{ cm}} = 5.5 \times 10^{37} \text{ erg s}^{-1}$. Using the 0.5–7 keV as an approximation for the 2–10 keV luminosity, the radio and X-ray fluxes are consistent with the radio-X-ray correlation, which is, e.g., shown by the corresponding projection of the fundamental plane of black hole activity in Merloni et al. (2003, left panel of their figure 3).

4.2 CO(1-0) kinematics and black hole mass

The CO(1-0) data for NGC 1277 are consistent with a scenario in which the CO(1-0)-emitting molecular gas is distributed in a ring corresponding to the dust lane (see Fig. 1). Since the beam size in the more compact configuration (at 2.5-arcsec resolution) is larger than the extent of the dust lane, the spatially-unresolved double-horned line profile seen in Fig. 5 suggests that CO emission is detected from the full extent of the dust lane. In Figs 11 and 12, we compare the CO(1-0) line profile to model predictions for different gas distributions and BH masses, based on a realistic model of the mass distribution in the centre of NGC 1277. According to the data by van den Bosch et al. (2012), the half-light radius is 1 kpc, and the total stellar mass is $1.2 \times 10^{11} M_\odot$. The distribution of light is such that a maximum of circular velocity of 476 km s^{-1} is reached at a radius of 0.56 kpc, when the mass-to-light ratio is selected as $M/L_V = 6.3$. This mass distribution corresponds also to the model of Emsellem (2013),

although the peak velocity is now 600 km s^{-1} , with a higher $M/L_V = 10$. We therefore adopted for the rotational velocity due to the stars the curve labelled “no BH” in figure 4 of Emsellem (2013), corresponding to the best multi-Gaussian expansion fit of the light distribution. To this stellar contribution, we added a point mass with two different values, as shown in Figs 11 and 12. For the molecular gas, we first assume a nuclear ring, corresponding to the dust lane. The ring is modelled using a constant surface density between 0.8 and 1.2 arcsec radii, or between 0.28 and 0.42 kpc. Since this distribution does not allow to sample the high velocities expected in the centre near the BH, we also consider another extreme molecular-gas distribution, which is an exponential disk with a scale of $r_0 = 50 \text{ pc}$, ending also at 0.42 kpc. For these two molecular gas distributions, we test two values for the BH mass, the high value of $1.7 \times 10^{10} M_\odot$ proposed by van den Bosch et al. (2012) and the lower value of $5 \times 10^9 M_\odot$ selected by Emsellem (2013). The inclination of the gas disk is assumed $i = 75^\circ$.

The combination of these scenarios yields 4 possible spectra, which we computed according to the model already used by Wiklind et al. (1997). For an assumed axisymmetric gas distribution of surface density $n(r)$, a typical global spectrum $dN/dv(V)$ is the sum over all radii r of

$$\frac{dN}{dv} dV = \int n(r) r dr d\theta = \int n(r) r dr \frac{dV}{V_{\text{rot}}(r) \sin \theta \sin i}, \quad (2)$$

where $V_{\text{rot}}(r)$ is the rotational velocity at radius r , and i the inclination of the galaxy in the sky ($i = 0$ is face-on). The observed velocity in each point is $V = V_{\text{rot}} \cos \theta \sin i$, and the global spectrum is derived by a simple radial integration. Fig. 11 shows the 4 spectra obtained when varying the BH mass and the adopted molecular gas distribution.

The simulation clearly shows that the most likely gas distribution is indeed the nuclear ring, corresponding to the dust lane. For the case of an exponential gas distribution, the velocity wings of the line are boosted, which is not observed.

If the molecular gas is distributed in the dust lane, the rotational velocities probe the total enclosed mass. The two horns of the observed CO(1-0) profile in Fig. 5 are roughly located at $V = \pm 500 \text{ km s}^{-1}$ with respect to the systemic velocity of NGC 1277. For an inclination of $i = 75^\circ$, this corresponds to a rotational velocity of $V_{\text{rot}} = V / \cos(90^\circ - i) \approx 520 \text{ km s}^{-1}$. The enclosed mass is given by $M_{\text{enc}} = (V_{\text{rot}}^2 r) / G$, where r is the distance of the gas from the BH and G is the gravitational constant. Using a distance of $r \sim 320 \text{ pc}$ (0.9 arcsec), corresponding to the radius of the dust lane, the resulting total enclosed mass is $M_{\text{enc}} \sim 2 \times 10^{10} M_\odot$. The models in Figs 11 and 12 provide a more detailed analysis by distinguishing the stellar and BH mass contributions. Compared to the line profile in Fig. 5, the best model for $M/L_V = 6.3$ (Fig. 11) appears to be the top left one, supporting the high mass for the BH. For $M/L_V = 10$ (Fig. 12), the width of the observed CO(1-0) spectrum can also be reproduced by the $5 \times 10^9 M_\odot$ BH (top right panel). We conclude that the observed CO(1-0) line profile is consistent with a $1.7 \times 10^{10} M_\odot$ BH, while a lower-mass $5 \times 10^9 M_\odot$ cannot be completely ruled out, if the underlying mass distribution is characterized by $M/L_V = 10$.

In the data at 1-arcsec spatial resolution, only the pronounced CO(1-0) component centred at $+500 \text{ km s}^{-1}$ is de-

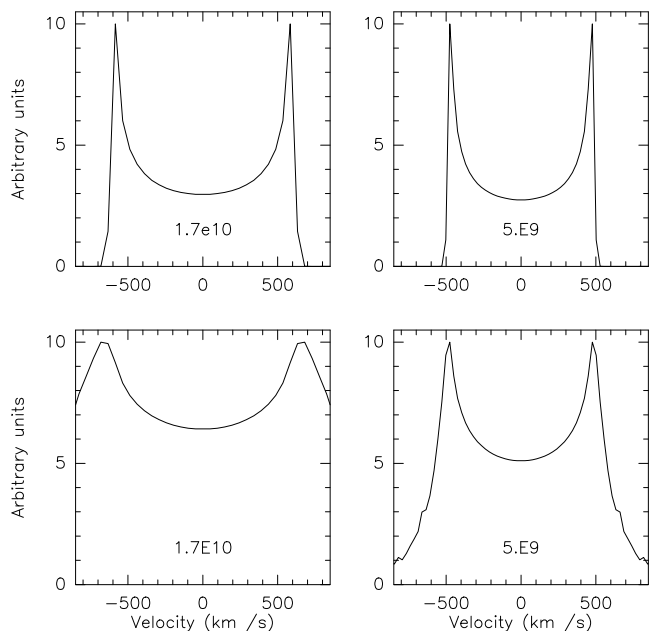


Figure 11. Molecular gas spectrum from the nuclear disk, computed assuming the van den Bosch et al. (2012) mass model for the stellar distribution with $M/L_V = 6.3$, and a black hole mass of $1.7 \times 10^{10} M_\odot$ (left) and $5 \times 10^9 M_\odot$ (right). The top two spectra correspond to a gas distribution in a ring, with constant surface density between 0.28 and 0.42 kpc (or 0.8 and 1.2 arcsec), and the bottom two spectra to a gas distribution in an exponential disk of characteristic scale 50 pc.

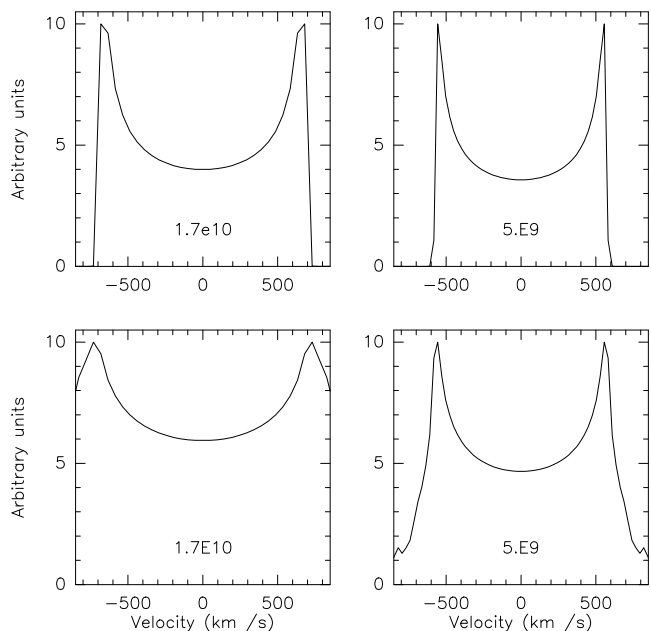


Figure 12. Same as Fig. 11, but now assuming $M/L_V = 10$.

tected. This emission peak is found to be offset by ~ 0.6 arcsec largely to the east of the 2.6-mm continuum peak. It is likely to be associated with a molecular gas clump close to the eastern orbital node of the dust lane. This interpretation is highlighted in comparison to the *HST* image in Fig. 13. While a blind comparison between the millimetre data and

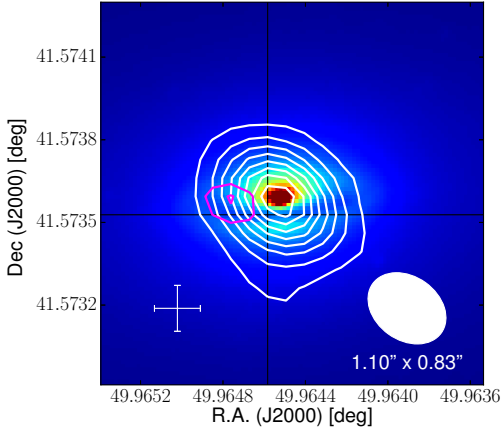


Figure 13. Overlay of the CO(1-0) line and 2.6-mm continuum emission found at 1-arcsec spatial resolution and the *HST* image. For this overlay, the astrometry of the *HST* image has been adjusted by hand in order to match the scenario, in which the 2.6-mm continuum peak is associated with the optical galaxy nucleus. The *HST* image is shown in colour scale. The continuum contours (white) are the same as in Fig. 2. The two CO(1-0) contours (magenta) are the same 4 and 5σ contours as shown in Fig. 6. The size and orientation of the beam corresponding to the continuum and CO(1-0) map is indicated in the lower right corner. The error bar in the lower left corner shows the estimated uncertainty of ± 0.3 arcsec in the absolute astrometry of the *HST* image.

the *HST* image is subject to the astrometric uncertainty of ~ 0.3 arcsec in the *HST* image, the astrometry in this Figure has been adjusted by hand in order to align the 2.6-mm continuum peak with the optical galaxy nucleus. The gas mass of this clump is $\sim 1 \times 10^7 M_{\odot}$, as derived from the flux measurement of $180 \text{ mJy km s}^{-1}$ (see Sect. 3.3) using equations 3 and 4 from Solomon & Vanden Bout (2005) with a Milky Way conversion factor of $\alpha = 4.6 M_{\odot} (\text{K km s}^{-1} \text{ pc}^2)^{-1}$. This gas mass is similar to the ones found for the most massive giant molecular clouds in the Milky Way (e.g. Murray 2011). This suggests that the component at $+500 \text{ km s}^{-1}$ could be associated with a single molecular cloud complex. For comparison, the total gas mass of the dust lane based on the CO(1-0) flux of 1850 to $2450 \text{ mJy km s}^{-1}$ found in the low-spatial-resolution data is $\sim (1.2 - 1.5) \times 10^8 M_{\odot}$, using the same conversion factors as above.

4.3 Implications for gas accretion onto the BH

If NGC 1277 hosts an ultra-massive BH of $M_{\text{BH}} \sim (1.3 - 1.7) \times 10^{10} M_{\odot}$, this BH is over-massive compared to the value expected from the fundamental plane of BH activity (Merloni et al. 2003), assuming that the radio continuum as well as the X-ray power-law source are indeed associated with an AGN. According to the fundamental plane relation from Gültekin et al. (2009b), the 6-cm radio luminosity of $5.5 \times 10^{37} \text{ erg s}^{-1}$ (see Section 4.1) combined with an approximate 2–10 keV luminosity of $1.3 \times 10^{40} \text{ erg s}^{-1}$ (Fabian et al. 2013, and Section 4.1) suggests a BH mass of about $1 \times 10^8 M_{\odot}$, which is two orders of magnitude smaller than the mass suggested by van den Bosch et al. (2012) and Yıldırım et al. (2015).

There is evidence that the gas accretion onto the BH in NGC 1277 deviates from simple Bondi accretion. Based on the thermal gas detected within the Bondi radius, Fabian et al. (2013) show that the accretion luminosity expected from radiatively efficient Bondi accretion is 5–6 orders of magnitude more luminous than the observed X-ray power-law component. As pointed out in Sect. 4.1, a similar order-of-magnitude difference is suggested by the 6-cm flux from Sijbring (1993), which is consistent with the radio-X-ray correlation as one projection of the fundamental plane of BH activity (though for a much smaller BH). Why the observed X-ray luminosity of the central point source in NGC 1277 is much smaller than the one expected for radiatively efficient Bondi accretion, remains unclear. Fabian et al. (2013) suggest the possibility of a very radiatively-inefficient accretion process. Alternatively, gas angular momentum may be responsible for lowering the accretion rate (Li et al. 2013).

The dust lane is likely to play an important role in impeding cold gas accretion. This has already been pointed out by Fabian et al. (2013), considering the high velocities in the dust lane that would be expected from the large BH mass. Our data support this picture, since the CO(1-0) detection is consistent with emission from a ring and shows the predicted high rotational velocities. While the gas in the dust lane may eventually lose angular momentum due to viscous processes and begin to spiral inward, the current lack of cold gas in the nuclear region may be the reason for the very low current BH accretion rate.

5 SUMMARY AND CONCLUSIONS

We have reported a detection of CO(1-0) emission from NGC 1277, probed at ~ 1 and ~ 2.5 arcsec spatial resolution, using the IRAM PdBI. The data indicate that the molecular gas is distributed in the ring of the dust lane encompassing the nucleus of NGC 1277 at a distance of 0.9 arcsec. Furthermore, the molecular gas shows high rotational velocities of $\sim 520 \text{ km s}^{-1}$. This is suggested both, by the low-resolution data, which reveal a very broad, double-horned, spatially unresolved line, covering a symmetric velocity range around the systemic velocity of NGC 1277, as well as by the high-resolution data, in which the strongest kinematic component centred at $\sim +500 \text{ km s}^{-1}$ is detected with an offset of ~ 0.6 arcsec to the east of the 2.6-mm continuum peak. The high rotational velocities of the molecular gas provide independent evidence for a central mass concentration of $\sim 2 \times 10^{10} M_{\odot}$ inside the radius of the dust lane. This enclosed mass is large enough to potentially host an ultra-massive BH as massive as reported by van den Bosch et al. (2012) and Yıldırım et al. (2015) based on stellar kinematics. Compared to models with realistic mass distributions for $M/L_V = 6.3$, the spatially-unresolved CO(1-0) line profile is consistent with the profile expected for the presence of a central $1.7 \times 10^{10} M_{\odot}$ BH. However, a lower-mass BH cannot be ruled out, if the stellar mass-to-light ratio is assumed to be high. The strong underlying 2.6-mm continuum emission of NGC 1277 cannot be explained by the cold dust component seen in the far-infrared. Based on literature X-ray and radio data, we suggest that the 2.6-mm continuum is caused by a weak AGN. The continuum

is extended and shows marginal evidence of an extension to the south that could be related to a radio-jet.

If the BH in NGC 1277 is as massive as $(1.3 - 1.7) \times 10^{10} M_{\odot}$, it appears to be an over-massive outlier, not only with respect to the BH-host galaxy scaling relations, but also regarding the fundamental plane of BH activity. It is likely that these peculiar properties are a result of the fact that NGC 1277 is located in the environment of the Perseus Cluster. It has been suggested that the formation of ultra-massive BHs may have proceeded rapidly in the early Universe, well before $z \sim 2-3$ (Dubois et al. 2012; Fabian et al. 2013). Early BH growth in NGC 1277 is supported by the fact that NGC 1277 seems to currently lack any significant BH accretion. The offset from the $M_{\text{BH}}-M_{\text{sph}}$ -relation indicates that NGC 1277 has either lost a large part of its stellar mass or has not been able to acquire additional stellar mass and gas after an initial phase of star formation. Furthermore, the lack of recent star formation, the currently small BH accretion rate, and the offset from the fundamental plane of BH activity suggest that NGC 1277 has been devoid of gas during its recent evolution. A stripping event in the cluster environment could have removed large parts of the gas and stellar mass, although this scenario has so far been regarded less likely (e.g. van den Bosch et al. 2012). If NGC 1277 has been moved off the $M_{\text{BH}}-M_{\text{sph}}$ -relation by tidal stripping, this implies that galaxies with ultra-massive BHs have been close to or in agreement with this relation by $z \sim 2-3$ and that ultra-massive BHs have primarily evolved in lockstep with their host galaxies. Alternatively, as suggested by Fabian et al. (2013), NGC 1277 may have undergone quenching at high redshift and may have been prevented from acquiring further gas and stellar mass by its off-centre location in the Perseus Cluster, in contrast to central cluster galaxies which may have grown significantly through mergers. In this case, NGC 1277 would have neither experienced galaxy nor BH growth in its more recent evolution and may be a ‘relic’ galaxy (Trujillo et al. 2014), in terms of both, its stellar population and BH. This scenario has recently been explored in more detail by Ferré-Mateu et al. (2015). As these authors discuss, this scenario implies that the growth of ultra-massive BHs may have preceded the growth of their host galaxies, so that all galaxies with ultra-massive BHs may have been outliers from the $M_{\text{BH}}-M_{\text{sph}}$ -relation by $z \sim 2-3$, in a similar manner as still observed for NGC 1277 today. It is noteworthy that the BH in the central galaxy of the Perseus Cluster, NGC 1275, is more than an order of magnitude less massive than the one suggested for NGC 1277 (Scharwächter et al. 2013). As a possible explanation, Shields & Bonning (2013) proposed that NGC 1277 may have captured a massive BH that had originally grown in NGC 1275.

Regardless of which process may have led to this particular BH distribution in NGC 1275 and NGC 1277, it is evident that probing the most massive BHs in clusters will provide new insights into cluster formation and evolution. Given the very small number of confirmed ultra-massive BHs to-date, future observations are required in order to better understand the growth of the most massive BHs and their host galaxies as well as the role of the cluster environment.

ACKNOWLEDGMENTS

Based on observations carried out under projects number X094 and W14DB with the IRAM Plateau de Bure Interferometer. IRAM is supported by INSU/CNRS (France), MPG (Germany) and IGN (Spain). We are grateful to the IRAM staff, especially Sabine König, for supporting the observations. J. S. and F. C. acknowledge the European Research Council for the Advanced Grant Program Num 267399-Momentum. This research has made use of the NASA/IPAC Extragalactic Database (NED) which is operated by the Jet Propulsion Laboratory, California Institute of Technology, under contract with the National Aeronautics and Space Administration.

REFERENCES

- Bertin E., Arnouts S., 1996, *A&AS*, **117**, 393
 Bertin E., Mellier Y., Radovich M., Missonnier G., Didelon P., Morin B., 2002, in Bohlender D. A., Durand D., Handley T. H., eds, *Astronomical Society of the Pacific Conference Series Vol. 281, Astronomical Data Analysis Software and Systems XI*. p. 228
 Busch G., et al., 2014, *A&A*, **561**, A140
 Cappellari M., Emsellem E., 2004, *PASP*, **116**, 138
 Cox P., Kruegel E., Mezger P. G., 1986, *A&A*, **155**, 380
 Davis T. A., 2014, *MNRAS*, **443**, 911
 Di Matteo T., Springel V., Hernquist L., 2005, *Nature*, **433**, 604
 Doi A., Kameno S., Kohno K., Nakanishi K., Inoue M., 2005, *MNRAS*, **363**, 692
 Doi A., Nakanishi K., Nagai H., Kohno K., Kameno S., 2011, *AJ*, **142**, 167
 Dowell C. D., et al., 2014, *ApJ*, **780**, 75
 Dubois Y., Pichon C., Haehnelt M., Kimm T., Slyz A., Devriendt J., Pogosyan D., 2012, *MNRAS*, **423**, 3616
 Emsellem E., 2013, *MNRAS*, **433**, 1862
 Fabian A. C., Sanders J. S., Haehnelt M., Rees M. J., Miller J. M., 2013, *MNRAS*, **431**, L38
 Falco E. E., et al., 1999, *PASP*, **111**, 438
 Ferrarese L., Merritt D., 2000, *ApJ*, **539**, L9
 Ferré-Mateu A., Mezcua M., Trujillo I., Balcells M., van den Bosch R. C. E., 2015, preprint, ([arXiv:1506.02663](https://arxiv.org/abs/1506.02663))
 Gebhardt K., et al., 2000, *ApJ*, **539**, L13
 Graham A. W., 2008, *ApJ*, **680**, 143
 Graham A. W., 2012, *ApJ*, **746**, 113
 Graham A. W., Scott N., 2013, *ApJ*, **764**, 151
 Graham A. W., Scott N., 2015, *ApJ*, **798**, 54
 Graham A. W., Onken C. A., Athanassoula E., Combes F., 2011, *MNRAS*, **412**, 2211
 Gültekin K., et al., 2009a, *ApJ*, **698**, 198
 Gültekin K., Cackett E. M., Miller J. M., Di Matteo T., Markoff S., Richstone D. O., 2009b, *ApJ*, **706**, 404
 Häring N., Rix H.-W., 2004, *ApJ*, **604**, L89
 Hlavacek-Larrondo J., Fabian A. C., Edge A. C., Hogan M. T., 2012, *MNRAS*, **424**, 224
 Högbom J. A., 1974, *A&AS*, **15**, 417
 Ichimaru S., 1977, *ApJ*, **214**, 840
 Jahnke K., Macciò A. V., 2011, *ApJ*, **734**, 92
 Kormendy J., Ho L. C., 2013, *ARA&A*, **51**, 511
 Kormendy J., Bender R., Cornell M. E., 2011, *Nature*, **469**, 374
 Lasker B. M., et al., 2008, *AJ*, **136**, 735
 Li J., Ostriker J., Sunyaev R., 2013, *ApJ*, **767**, 105
 Magorrian J., et al., 1998, *AJ*, **115**, 2285
 Marconi A., Hunt L. K., 2003, *ApJ*, **589**, L21
 Mathur S., Fields D., Peterson B. M., Grupe D., 2012, *ApJ*, **754**, 146

- McConnell N. J., Ma C.-P., 2013, *ApJ*, **764**, 184
- McConnell N. J., Ma C.-P., Gebhardt K., Wright S. A., Murphy J. D., Lauer T. R., Graham J. R., Richstone D. O., 2011, *Nature*, **480**, 215
- McConnell N. J., Ma C.-P., Murphy J. D., Gebhardt K., Lauer T. R., Graham J. R., Wright S. A., Richstone D. O., 2012, *ApJ*, **756**, 179
- Merloni A., Heinz S., di Matteo T., 2003, *MNRAS*, **345**, 1057
- Mink D. J., 1997, in Hunt G., Payne H., eds, *Astronomical Society of the Pacific Conference Series Vol. 125, Astronomical Data Analysis Software and Systems VI*. p. 249
- Murray N., 2011, *ApJ*, **729**, 133
- Peng C. Y., 2007, *ApJ*, **671**, 1098
- Sani E., Marconi A., Hunt L. K., Risaliti G., 2011, *MNRAS*, **413**, 1479
- Savorgnan G. A. D., Graham A. W., 2015, *MNRAS*, **446**, 2330
- Scharwächter J., McGregor P. J., Dopita M. A., Beck T. L., 2013, *MNRAS*, **429**, 2315
- Shields G. A., Bonning E. W., 2013, *ApJ*, **772**, L5
- Sijbring D., 1993, PhD thesis, University of Groningen
- Silk J., Rees M. J., 1998, *A&A*, **331**, L1
- Solomon P. M., Vanden Bout P. A., 2005, *ARA&A*, **43**, 677
- Sun M., Jones C., Forman W., Vikhlinin A., Donahue M., Voit M., 2007, *ApJ*, **657**, 197
- Trujillo I., Ferré-Mateu A., Balcells M., Vazdekis A., Sánchez-Blázquez P., 2014, *ApJ*, **780**, L20
- Volonteri M., Ciotti L., 2013, *ApJ*, **768**, 29
- Wiklund T., Combes F., Henkel C., Wyrowski F., 1997, *A&A*, **323**, 727
- Winge C., Riffel R. A., Storchi-Bergmann T., 2009, *ApJS*, **185**, 186
- Yıldırım A., van den Bosch R., van de Ven G., Husemann B., Lyubenova M., Walsh J. L., Gebhardt K., Gültekin K., 2015, preprint, ([arXiv:1506.06762](https://arxiv.org/abs/1506.06762))
- Yun M. S., Reddy N. A., Condon J. J., 2001, *ApJ*, **554**, 803
- van den Bosch R. C. E., Gebhardt K., Gültekin K., van de Ven G., van der Wel A., Walsh J. L., 2012, *Nature*, **491**, 729

This paper has been typeset from a $\text{T}_{\text{E}}\text{X}/\text{L}^{\text{A}}\text{T}_{\text{E}}\text{X}$ file prepared by the author.